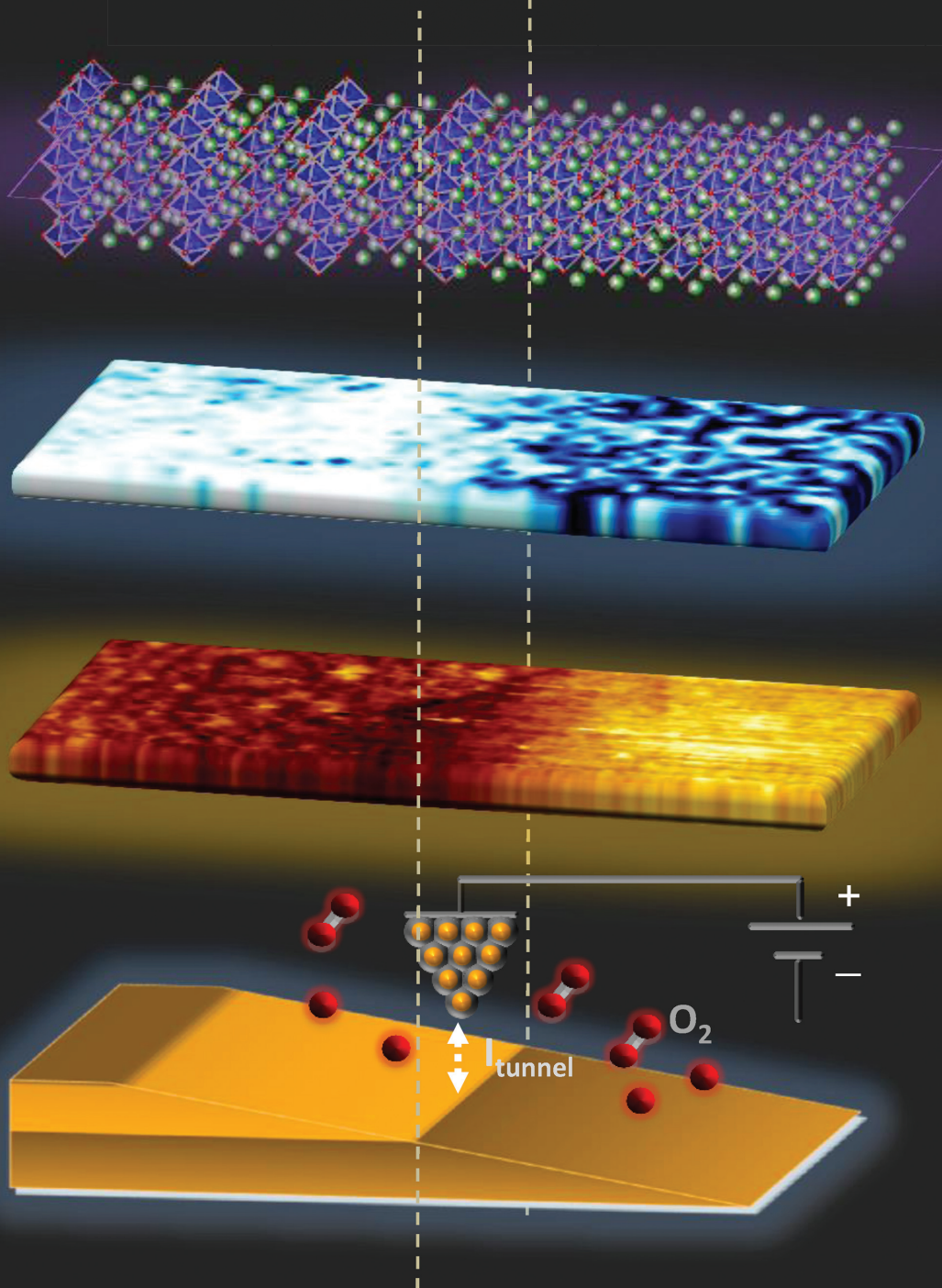


# ADVANCED ENERGY MATERIALS



# Electronic Activation of Cathode Superlattices at Elevated Temperatures – Source of Markedly Accelerated Oxygen Reduction Kinetics

Yan Chen, Zhuhua Cai, Yener Kuru, Wen Ma, Harry L. Tuller, and Bilge Yildiz\*

Solid-oxide fuel cells are an attractive energy conversion technology for clean electric power production. To render them more affordable, discovery of new cathode materials with high reactivity to oxygen reduction reaction (ORR) at temperatures below 700 °C is needed. Recent studies have demonstrated that  $\text{La}_{0.8}\text{Sr}_{0.2}\text{CoO}_3/(\text{La}_{0.5}\text{Sr}_{0.5})_2\text{CoO}_4$  ( $\text{LSC}_{113/214}$ ) hetero-interfaces exhibit orders of magnitude faster ORR kinetics compared with either single phase at 500 °C. To obtain a microscopic level understanding and control of such unusual enhancement, we implemented a novel combination of in situ scanning tunneling spectroscopy and focused ion beam milling to probe the local electronic structure at nanometer resolution in model multilayer superlattices. At 200–300 °C, the  $\text{LSC}_{214}$  layers are electronically activated through an interfacial coupling with  $\text{LSC}_{113}$ . Such electronic activation is expected to facilitate charge transfer to oxygen, and concurrent with the anisotropically fast oxygen incorporation on  $\text{LSC}_{214}$ , quantitatively explains the vastly accelerated ORR kinetics near the  $\text{LSC}_{113/214}$  interface. Our results contribute to an improved understanding of oxide hetero-interfaces at elevated temperatures and identify electronically coupled oxide structures as the basis of novel cathodes with exceptional performance.

## 1. Introduction

The oxygen reduction reaction governs the performance of a range of electrochemical energy conversion devices such as fuel cells and batteries.<sup>[1,2]</sup> Extensive efforts have been directed towards understanding the oxygen reduction mechanism, and hence to guide the design of high performance electrocatalysts.<sup>[3,4]</sup> For Solid Oxide Fuel Cells (SOFCs), in particular, synthesizing cathode materials with high ORR activity at

intermediate temperatures (<700 °C) is necessary to obtain devices with long life and reduced cost.<sup>[2]</sup> Traditional approaches for enhancing cathode performance include tailoring of crystal structure, chemical composition, and microstructure, including the use of porous nanostructured composites.<sup>[5]</sup> Recent reports of oxide hetero-structures, exhibiting exceptionally high ORR activity and ionic conductivity, promise an alternative approach for achieving high-performance cathodes.<sup>[6–10]</sup> A prime example is the  $(\text{La},\text{Sr})\text{CoO}_3/(\text{La},\text{Sr})_2\text{CoO}_4$  ( $\text{LSC}_{113/214}$ ) hetero-structure, for which spatially resolved secondary ion mass spectrometry (SIMS) demonstrated three to four orders of magnitude faster oxygen exchange kinetics near the interfaces between  $\text{LSC}_{113}$  and  $\text{LSC}_{214}$  thin layers at about 500 °C compared to either material individually.<sup>[7,10]</sup> Such astonishing improvement of oxygen exchange kinetics was confirmed by electrochemical measurements, in both

dense thin film<sup>[9]</sup> and porous<sup>[8]</sup> structures. It is evident that the interfacial regions of these  $\text{LSC}_{214/113}$  hetero-structures are responsible for such impressively accelerated ORR kinetics. However, the physical origin of these empirically observed results remains obscure to date. Obtaining a fundamental and microscale understanding of the role of these special interfaces is essential for the future design of novel cathode structures. In this work, we report the discovery of the high-temperature electronic activation of a wide-band-gap oxide,  $\text{LSC}_{214}$ , by an adjacent smaller-band-gap material  $\text{LSC}_{113}$ , as a model system, and the elucidation of this behavior in accelerating the ORR kinetics.

$\text{LSC}_{113}$  is a widely-studied SOFC cathode with high electronic and ionic conductivity.<sup>[11]</sup> It can be easily reduced and forms electronic defect states that facilitate electron transfer to adsorbing oxygen species on its surface.<sup>[12]</sup> Oxygen reduction on  $\text{LSC}_{113}$  is primarily limited by the availability and mobility of surface oxygen vacancies.<sup>[13]</sup> On the other hand,  $\text{LSC}_{214}$ , as shown in our recent theoretical work,<sup>[14]</sup> exhibits very high oxygen incorporation and oxygen diffusion kinetics on the (100) plane, due to its capability to accommodate oxygen interstitials within the rock salt layers (between the AO-AO planes). This anisotropic behavior is similar to the case demonstrated experimentally for

Y. Chen, Dr. Z. Cai, Dr. Y. Kuru, W. Ma,  
Prof. B. Yildiz  
Laboratory for Electrochemical Interfaces  
Department of Nuclear Science and Engineering  
Massachusetts Institute of Technology  
77 Massachusetts Avenue  
Cambridge, MA 02139, USA  
E-mail: byildiz@mit.edu  
Dr. Y. Kuru, Prof. H. L. Tuller  
Department of Materials Science and Engineering  
Massachusetts Institute of Technology  
77 Massachusetts Avenue, Cambridge, MA 02139, USA



DOI: 10.1002/aenm.201300025

other Ruddlesden-Popper (RP) phase materials with the  $A_2BO_4$  structure.<sup>[15–17]</sup> However, because of the reduced symmetry of its crystal structure,  $LSC_{214}$  has a lower bulk electronic conductivity than  $LSC_{113}$  ( $\sim 1700 \text{ S cm}^{-1}$  for  $La_{0.8}Sr_{0.2}CoO_3$ <sup>[18]</sup> and  $\sim 120 \text{ S cm}^{-1}$  for  $(La_{0.5}Sr_{0.5})_2CoO_4$ <sup>[19]</sup> at  $600^\circ\text{C}$  in air), and a larger band gap, as demonstrated later in this paper. At intermediate temperatures, the ORR on many RP phase cathode materials, including  $LSC_{214}$ ,<sup>[20]</sup>  $Nd_2NiO_4$ ,<sup>[21]</sup> and  $(La,Sr)_2MnO_4$ ,<sup>[22]</sup> was reported to be mainly limited by charge transfer from the oxide surface to the adsorbed oxygen. This behavior likely arises from the low electronic conductivity, large band gap and deficiency in the concentration of conduction band electrons on the surface of these materials. Based on the facts above, we hypothesize that the mechanism that renders the  $LSC_{214/113}$  hetero-interface orders of magnitude more highly reactive to ORR than either phase individually is that it combines the desirable features of  $LSC_{113}$  and  $LSC_{214}$  through a coupling at the interface of these two phases – namely, the availability of electrons in  $LSC_{113}$  for the reduction of surface species, and the fast oxygen incorporation kinetics on the (100) surface of  $LSC_{214}$ .

The objective of this work is to understand the origin of the local oxygen reduction activity on the basis of the local electronic structure near the  $LSC_{113/214}$  interface at conditions close to that of the functional environment of SOFCs. Major challenges in achieving this understanding are related to two key aspects: a) the ability to probe the electronic structure confined at the nano-meter scale near an interface, which has been a well-known complication in the study of hetero-interfaces,<sup>[23,24]</sup> and b) performing such experiments *in situ* at high temperature and in an oxygen environment. In our work, we implement a novel combination of *in situ* scanning tunneling microscopy and spectroscopy (STM/STS) and grazing incidence focused ion beam (FIB) milling. This capability, for the first time, enables us not only to probe the electronic structure across hetero-interfaces with nano-scale resolution, but also to perform these measurements at high temperature and in an oxygen/gas environment. Scanning probe techniques are ideal in revealing local electronic, magnetic or electrochemical properties on the surface.<sup>[25–29]</sup> Nevertheless, challenges arise when attempting to apply them to interrogate interfaces of multilayers buried beneath the surface<sup>[30]</sup> and under the harsh working conditions of SOFC cathodes (high temperatures and in oxygen environments). Previous successful attempts at exposing the local interface properties of oxides to scanning probe characterization<sup>[26,27]</sup> have not provided a generalized capability to expose buried interfaces in a controllable fashion and have been limited to room temperature measurements. As we show in this paper,  $LSC_{214}$  is electronically activated when it interfaces with  $LSC_{113}$  at high temperature. Such activation is reversible with temperature—that is, it cannot be captured by traditional techniques at room temperature, or even by heating and then quenching samples to room temperature for measurement, and requires *in situ* probes for identifying the electronic structure of the surfaces at elevated temperatures.

Our *in situ* approach enabled us to visualize an electronic structure transition over a 1 nm-thick interfacial zone between  $LSC_{113}$  and  $LSC_{214}$  layers in a nano-scale multilayer (ML) structure at room temperature, and to discover the high-temperature electronic activation on the surface of the wide-band-gap oxide  $LSC_{214}$  layers. This finding, we believe, provides new and important physical insights into the extremely high ORR activity of the dissimilar interfaces between  $LSC_{214}$  and  $LSC_{113}$ . It further supports the notion that electronic activation of  $LSC_{214}$ , coupled with fast oxygen incorporation kinetics on its (100) surface, is one governing factor for the fast oxygen reduction kinetics of  $LSC_{113/214}$  interfaces by facilitating charge transfer during oxygen adsorption. Lastly, our work identifies “electronically coupled oxide hetero-structures” as a new basis of high-performance SOFC cathodes, and heralds a novel approach to the design of cathode structures utilizing electronic coupling at oxide hetero-interfaces at elevated temperature.

## 2. Results and Discussion

### 2.1. Structure and Composition of the Model Multilayers

Super-lattices made of 10 nm-thick  $La_{0.8}Sr_{0.2}CoO_3$  ( $LSC_{113}$ ) and  $(La_{0.5}Sr_{0.5})_2CoO_4$  ( $LSC_{214}$ ) layers with 10 modulations were grown on  $SrTiO_3$  (STO) (001) substrates by pulsed laser deposition. Both the  $LSC_{214}$  and  $LSC_{113}$  layers in the ML structure were highly textured in the [001] out of plane direction, as shown in supporting materials Figure S1. The strain states of multiple ML structures synthesised in this work were found to range from no strain (Figure S1 (a)) to a compressive strain of  $-0.5\%$  for  $LSC_{113}$  and a tensile strain of  $+1\%$  for  $LSC_{214}$  in the [001] direction (Figure S1(b)). The results presented below are from the unstrained ML structure. This serves to isolate the direct chemical and electronic effects that arise at the  $LSC_{113/214}$  interface, and avoids complexities that may arise due to the role of lattice strain in influencing oxygen vacancy formation and mobility.<sup>[14,31]</sup>

By using grazing incidence FIB milling, the buried interfaces and layers in the ML structure were exposed on the surface (illustrated in Figure 1(a), (b) and (c)) to facilitate STM/STS

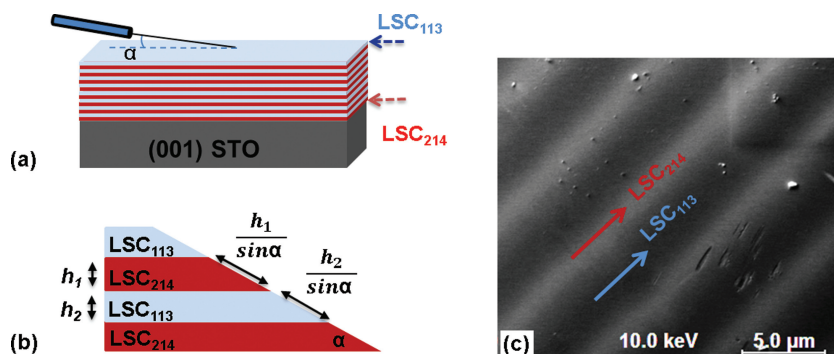


**Figure 1.** Illustration of Focus Ion Beam milling process on the  $LSC_{214/113}$  multilayer (ML) structure and characterization of exposed interface. (a) Geometry of the FIB milling process (b) The cross-sectional view of the multilayer after the FIB milling, illustrating the spatial magnification of each layer on the newly formed surface. (c) Scanning electron microscopy (SEM) image of the  $LSC_{113/214}$  ML cross-section following FIB milling.



characterization.<sup>[30]</sup> After FIB sectioning, Ar<sup>+</sup> ion sputtering was used to remove any potential Ga implantation, followed by annealing to recover any potential radiation damage. As shown in Figure S2 (b), the auger electron spectroscopy (AES) measurements confirmed that there is no residual Ga on the FIB milled region. The surface cation composition of the LSC<sub>113</sub> on the top surface layer and on the exposed cross-section of the ML region were found to be the same, within the quantification error limits of the high-spatial-resolution AES measurement, as shown in Figure S2 (c, d). This suggests that the FIB milling does not induce discernible changes in the material properties. In a parallel ongoing work in our group,<sup>[32]</sup> we have grown LSC<sub>113/214</sub> vertically aligned nano-composite (VAN) thin films, in which the LSC<sub>113</sub> and LSC<sub>214</sub> phases separate into vertically aligned and highly textured ((001) direction) columnar domains of 200–300 nm dimension during pulsed laser deposition. FIB milling is not used in the preparation of the VAN structure. The electronic activation of LSC<sub>214</sub> on the VAN surface was also found at elevated temperature and akin to the results we report on the multilayer structure here. This finding also confirms that the results we observed in this study are not a chemical artifact of the FIB milling process. The quantitative differences in Sr intensity measured by AES line scan across the interface are consistent with the formation of distinct LSC<sub>113</sub> and LSC<sub>214</sub> phases in the multilayer structure (Figure S2 (e)).

## 2.2. Electronic Structure from Room Temperature to Elevated Temperatures

The topography measured by STM (left) and the tunneling current map (right) near an interface of the LSC<sub>113/214</sub> ML system at room temperature are shown in Figure 2(a). Two distinct electronic regions are clear from the tunneling current map (Figure 2(a)) and from the individual tunneling spectra exemplified in Figure 2(b). The energy gap values are found to be  $1.4 \pm 0.2$  eV on the LSC<sub>113</sub> layers and  $2.6 \pm 0.3$  eV on the LSC<sub>214</sub> layers. The energy gap of LSC<sub>113</sub> in this ML structure is consistent with the energy gap value that we previously reported as  $1.5 \pm 0.2$  eV at room temperature on the surface of LSC<sub>113</sub> single phase epitaxial thin films grown on STO (001).<sup>[12]</sup>

A gradual transition in the electronic structure from the LSC<sub>113</sub> to the LSC<sub>214</sub> phase in the ML structure is clear in Figure 2(b). By using low angle FIB milling, we magnified the “apparent” scale of the transition region from about 1 nm to 200 nm, the latter dimension feasibly captured in cross-sectional STM/STS. This novel approach can be extended to the study of electronic structure near hetero-interfaces for other oxide ML systems, such as those studied for electronic and magnetic property modulations.<sup>[24,27,33]</sup> The identified transition region can arise due to tunneling from the layer underneath, redistribution of dopant cations (e.g. Sr),<sup>[34]</sup> oxygen vacancies<sup>[35]</sup> and electronic carriers<sup>[36]</sup> within a space charge zone near

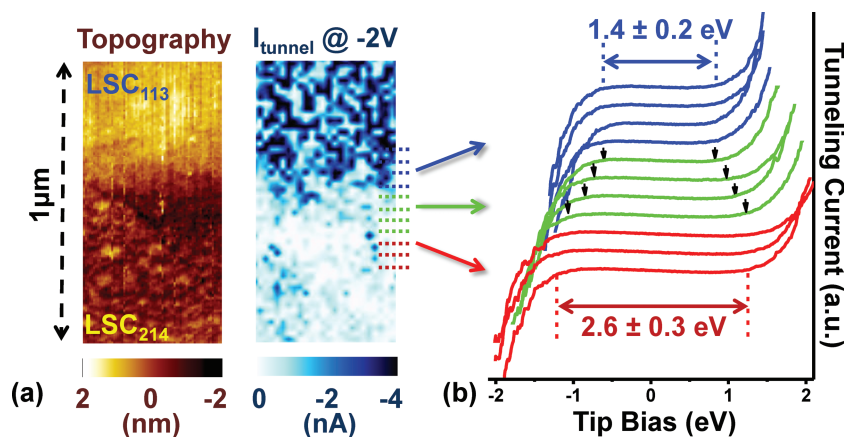


**Figure 2.** Transition region across the LSC<sub>214/113</sub> interface detected by scanning tunneling microscopy/spectroscopy (STM/STS) at room temperature. (a) Topography image (left) by STM, and tunneling current map (right) by STS at  $V_{\text{tip}} = -2$  V. (b) Evolution of tunneling current vs. bias behavior across the LSC<sub>214/113</sub> interface. The spectra in blue and red are in the LSC<sub>214</sub> and LSC<sub>113</sub> layers, respectively. The spectra in green are measured at the transition region, which is about 200 nm wide (about 1 nm real thickness) in this FIB-cut geometry.

the interface or electronic reconstruction near the interface (Figure S3).<sup>[24]</sup> Regardless of the governing mechanism, the lateral spread of this effect over only 1 nm is too narrow compared with the spatial extent of the high oxygen exchange activity for the LSC<sub>113/214</sub> interfaces shown with SIMS.<sup>[7,10]</sup>

At elevated temperatures, the electronic structure contrast between the two phases, as measured by STS, was found to diminish (Figure 3). At room temperature (RT), a large contrast in the tunneling current maps between the LSC<sub>113</sub> and LSC<sub>214</sub> phases is clear and correlates well with the spatial transitions in the STM images. Interestingly, the energy gaps of both phases decrease and disappear similarly with increasing temperature, contrary to the behavior of the single-phase LSC<sub>214</sub> thin film. The transition from the presence of an energy gap with large contrast between the two phases at room temperature to a metallic-like state in both the LSC<sub>113</sub> and LSC<sub>214</sub> layers of the ML structure at about 250 °C is reversible. When the samples are cooled back to RT after being heated to 300 °C, the energy gap of both phases return to their initial values (Figure 4). Because of the reversibility of these transitions, this behavior can only be captured with *in situ* measurements.

It is evident that the LSC<sub>113</sub> surface electronic structure in the ML structure behaves very similarly to its single-phase counterpart at high temperatures<sup>[12]</sup> (shown up to 300 °C in Figure 4(a)). On the other hand, the electronic structure of LSC<sub>214</sub> in the ML differs significantly by showing a reversible disappearance of the energy gap at and above 250 °C (Figure 4(b)). As mentioned above, the LSC<sub>214</sub> single phase thin film was too insulating for STM/STS measurements at room temperature, thus, an energy gap value is not reported specifically at RT before and after the high-temperature experiments. The energy gap of the LSC<sub>214</sub> phase in the ML structure was  $2.6 \pm 0.3$  eV at RT; larger than that of the LSC<sub>113</sub> phase ( $1.5 \pm 0.2$  eV) both in the ML structure and in single phase thin film form. At 200 °C, the LSC<sub>214</sub> energy gap in the ML structure decreases to  $1.6 \pm 0.2$  eV, close to the energy gap of the LSC<sub>214</sub> single phase thin film at the same temperature. However, upon



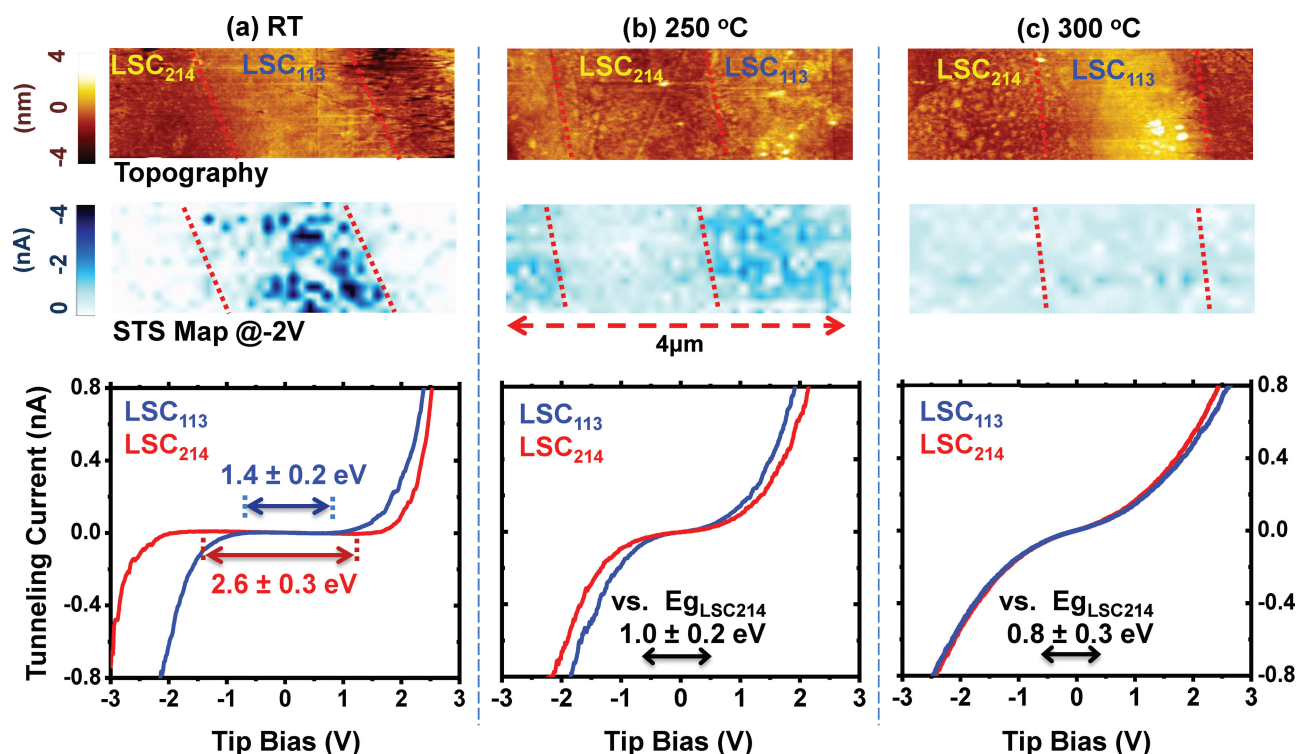


**Figure 3.** Topography and tunneling current map at  $V_{\text{tip}} = -2$  V from room temperature (RT) to 300 °C under oxygen pressure of  $10^{-3}$  mbar. (a) at RT: a large energy gap exists in the tunneling spectra in both the LSC<sub>113</sub> and LSC<sub>214</sub> layers within the ML structure, and the contrast shown in the tunneling current map reflects the distinct electronic structures between the LSC<sub>113</sub> and LSC<sub>214</sub> phases. (b) at 250 °C: no evident energy gap is present in the tunneling spectra of LSC<sub>113</sub> and LSC<sub>214</sub> phase, and the spatial contrast in the tunneling conductance decreases compared to that at RT. (c) at 300 °C: no evident energy gap is present in the tunneling spectra of LSC<sub>113</sub> and LSC<sub>214</sub> phase, and no difference between the electronic structure of LSC<sub>113</sub> and LSC<sub>214</sub> layers is detected within the bias range shown in the I-V plots.  $E_{\text{g,LSC214}}$  on the I-V plots in (b) and (c) represents the energy gap values measured on the single phase LSC<sub>214</sub> film surfaces, and are compared here to the results obtained from the LSC<sub>214</sub> layers in the ML structure.

further increase in temperature to 250 °C, the energy gap of the LSC<sub>214</sub> in the ML structure disappears in contrast to that of the single phase LSC<sub>214</sub> thin film which exhibits an apparent energy gap of  $1.0 \pm 0.2$  eV at 250 °C and  $0.8 \pm 0.3$  eV at 300 °C.

In light of these observations, we assess the possible mechanism of how the presence of LSC<sub>113</sub> influences the LSC<sub>214</sub>

electronic structure and activates it electronically through a coupling at their interface. In particular, we focus on the oxygen vacancy defect states and the injection of associated excess electrons from LSC<sub>113</sub> into LSC<sub>214</sub>. We have previously shown that LSC<sub>113</sub> thin film surfaces begin to lose oxygen and form oxygen vacancies at 200–300 °C.<sup>[12]</sup> These oxygen vacancies modify the

*d* band structure of the neighboring transition metal cations and create defect states within the gap,<sup>[37]</sup> leading to the decrease and disappearance of the surface energy gap on LSC<sub>113</sub>.<sup>[12]</sup> The same phenomenon was also demonstrated for La<sub>0.7</sub>Sr<sub>0.3</sub>MnO<sub>3</sub><sup>[38]</sup> and Sr(Ti,Fe)O<sub>3</sub><sup>[39]</sup> thin films in our recent work. Because the LSC<sub>113</sub> surface energy gap changes in a similar way with temperature in the ML and single phase thin films, its decrease and disappearance in the ML is also likely due to the creation of oxygen vacancies in its near surface region. However, the reduction enthalpy in the LSC<sub>214</sub> is considered to be higher than that in LSC<sub>113</sub>, consistent with the fact that LSC<sub>214</sub> accommodates interstitial oxygen defects rather than oxygen vacancies in air for Sr content equal to or smaller than 50% on the A-site.<sup>[14,19]</sup> To

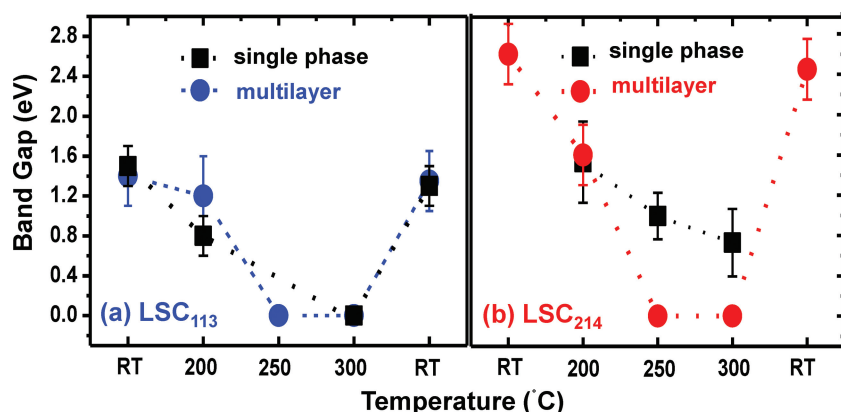


**Figure 4.** Comparison of the apparent energy gap as a function of temperature. Energy gap values obtained on (a) LSC<sub>113</sub> and (b) LSC<sub>214</sub> when they are within the ML structure versus values obtained for the single phase thin film structure. The data on the single phase LSC<sub>113</sub> films come from our previous report.<sup>[12]</sup>

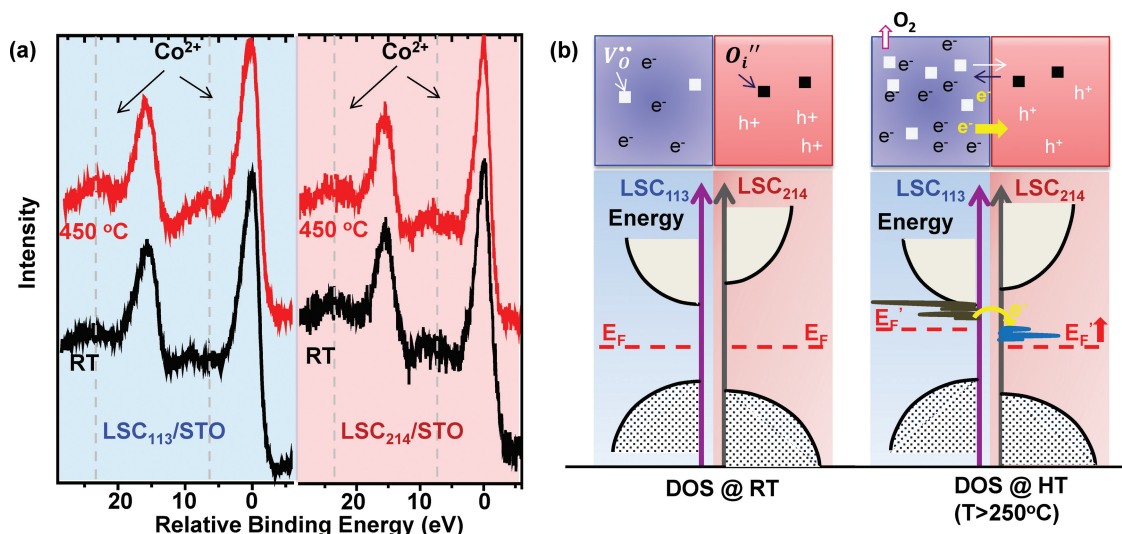


**Figure 5.** Co 2p photoelectron spectra for assessing the oxygen vacancy formation ease on LSC<sub>113</sub> and LSC<sub>214</sub>, and the illustration of electron injection from oxygen vacancy defect states of LSC<sub>113</sub> into LSC<sub>214</sub>. (a) Comparison of the Co 2p spectra on the LSC<sub>113</sub> single phase thin film (data from authors' previous work<sup>[12]</sup>) and on the LSC<sub>214</sub> single phase thin film on STO substrates as a function of temperature at ultra-high vacuum ( $\sim 10^{-9}$  mbar). (b) Illustration of how the presence of reduced LSC<sub>113</sub> surface can affect the LSC<sub>214</sub> electronic structure through a coupling at their interface in the ML structure: upon the creation of oxygen vacancies, excess electrons in LSC<sub>113</sub> are injected from LSC<sub>113</sub> to LSC<sub>214</sub>. (Top) Electron injection is expected to be accompanied by the exchange of positively charged oxygen vacancies and negatively charged oxygen interstitials across the interface on the surface. (Bottom) Creation of oxygen vacancies liberates electrons and forms defect states in the energy gap, raises the Fermi level in LSC<sub>113</sub>, and thus, enables the injection of electrons into LSC<sub>214</sub>. The last step raises the Fermi level in LSC<sub>214</sub>. DOS stands for density of states; RT and HT refer to room temperature and high temperature.

confirm this, we compared the valence state of the Co cation in relation to the oxygen vacancy formation process in these two phases. A significant reduction of Co on the LSC<sub>113</sub> film surface is evident from the appearance of the Co<sup>2+</sup> satellite peak at about 300 °C (Figure 5(a)), coincident with the temperature at which its surface energy gap was found to disappear (Figure 4a). On the contrary, the Co 2p spectrum on the LSC<sub>214</sub> (Figure 5a) does not change between 200 to 300 °C. These results demonstrate that the formation of oxygen vacancies and the reduction of Co in the LSC<sub>214</sub> phase are more difficult than that in the LSC<sub>113</sub> phase. This is consistent with our theoretical findings which show that the oxygen vacancy formation energy is much higher on LSC<sub>214</sub> compared to that on LSC<sub>113</sub> (Figure S5 (a)).<sup>[14]</sup> Therefore, the disappearance of the energy gap on the LSC<sub>214</sub> layers in the ML structure cannot occur due to oxygen vacancy formation and reduction of Co within LSC<sub>214</sub> at 200–300 °C (Figure 5a).

Based on the results of the Co valence state and electronic structure on the LSC<sub>113</sub> and LSC<sub>214</sub> layers as a function of temperature, we propose that the electronic activation of LSC<sub>214</sub> in the ML structure is caused by injection of electrons from LSC<sub>113</sub> to LSC<sub>214</sub> across their interface, as illustrated in Figure 5(b). Excess electrons in the lattice accompany the creation of oxygen vacancy defects on transition metal oxides, thereby decreasing the electronegativity of the surface.<sup>[40]</sup> Given the easier oxygen vacancy formation on LSC<sub>113</sub>, the reduction in electronegativity (and raising of the Fermi level) is expected to be larger for LSC<sub>113</sub> as compared to that for LSC<sub>214</sub> at high temperatures. Such difference in the relative change in electronegativity could result in a band alignment as illustrated in Figure 5(b) and lead to electron injection from LSC<sub>113</sub> to LSC<sub>214</sub>. This is

accompanied by the Fermi level rising into the conduction band of LSC<sub>214</sub>, leading to the apparent disappearance of the surface energy gap.

Lastly, it is important to note that at 300 °C, the entire extent of the LSC<sub>214</sub> layers is activated by adjacent LSC<sub>113</sub> layers within the multilayer structure. This indicates that the spatial extent of the activated region in LSC<sub>214</sub> is at least the film thickness of 10 nm. On the VAN structured thin films,<sup>[32]</sup> in which the LSC<sub>113</sub> and LSC<sub>214</sub> columnar domains are of 200–300 nm lateral dimensions, we observed the same electronic activation of the entire LSC<sub>214</sub> domains. This demonstrates that the spatial extent of activation on LSC<sub>214</sub> is at least on the order of hundred nm. While such a large spatial extent of electronic activation is contrary to the narrowly confined space charge zones that normally form at the interface of heavily doped dissimilar semiconductors without mobile charged donor and acceptor species,<sup>[41]</sup> we have the following consistent explanation for the system in hand. As mentioned, LSC<sub>113</sub> loses oxygen at elevated temperature, resulting in the formation of positively charged oxygen vacancies, accompanied by the donation of electrons to the conduction band. On the other hand, negatively charged oxygen interstitials form in LSC<sub>214</sub>,<sup>[17]</sup> accompanied by the formation of holes in the valence band. Unlike the dopant cations that are immobile in conventional semiconductors, e.g. as in GaAs-InAs heterostructures,<sup>[42]</sup> the oxygen vacancies and interstitials are capable of migrating in the vicinity of the LSC<sub>113/214</sub> interface region under a chemical potential gradient and at elevated temperatures. Thus electron injection from LSC<sub>113</sub> to LSC<sub>214</sub> should be accompanied by the corresponding migration of oxygen vacancies and oxygen interstitials across the interface, thereby maintaining charge neutrality in both

phases, but in the presence of an altered defect chemistry in each layer. And because these intrinsic donor and acceptor species can migrate relatively long distances in the oxide films, a larger spatial scale of electronic activation region in  $\text{LSC}_{214}$  is reasonably expected, compared to traditional semiconductor heterostructures.

### 2.3. Implications for Oxygen Reduction Activity

We assessed the possible magnitude of ORR activity enhancement that can be expected on the basis of our electronic structure findings on the  $\text{LSC}_{214/113}$  system. Electron transfer from oxide surface to adsorbed oxygen is reported to be the rate-limiting ORR process on the  $\text{LSC}_{214}$  cathode at reduced temperatures,<sup>[20]</sup> similar to the reports on other  $\text{A}_2\text{BO}_4$  structured cathode materials.<sup>[21,22]</sup> The ease of charge transfer from a wide-band-gap oxide, such as  $\text{LSC}_{214}$ , to adsorbed oxygen is governed, in part, by the number of electrons in the conduction band available at its surface.<sup>[4]</sup> This quantity is exponentially dependent on the energy distance between the Fermi level  $E_F$  and bottom of the conduction band  $E_C$ , represented as in equation (1), where  $N_C$  is the effective density of states and  $n$  is the electron density in the conduction band.

$$n = N_C e^{-\frac{E_C - E_F}{k_B T}} \quad (1)$$

The reduction in  $E_C - E_F$  represents a decrease in the energy barrier to transfer charge from the surface to oxygen on wide-band-gap oxide cathodes.<sup>[4]</sup> At 300 °C and under  $10^{-3}$  mbar of oxygen pressure, the energy difference between the Fermi level and the bottom of conduction band on single phase  $\text{LSC}_{214}$  is about 0.4 eV, as shown in Figure 6. For the same conditions, no energy gap was observed on  $\text{LSC}_{214}$  in the ML structure. This is equivalent to a 0.4 eV decrease of the charge transfer energy barrier at the surface. Assuming an Arrhenius behavior, a  $10^3$  times increase in the rate of charge transfer to oxygen is expected. This orders-of-magnitude increase is comparable to the increase in oxygen reduction kinetics reported by refs.<sup>[7–10]</sup> We note that the conditions in our STM/STS measurement, up to 300 °C and under oxygen pressure of  $10^{-3}$  mbar in this work, provide an oxygen chemical potential of  $-1.85$  eV, which is equivalent to the conditions of 470 °C and  $10^{-2}$  bar, and of 590 °C and 1 bar (Figure S6). The latter conditions are close to those of the experiments reported in refs.<sup>[7–10]</sup> Therefore, based on our assessment of ORR activity enhancement under these conditions, the electronic activation effects can explain, at least in part, the origin of the orders of magnitude improvement of ORR kinetics reported in refs.<sup>[7–10]</sup>

Theoretical work from our group<sup>[14]</sup> predicts  $10^2$  times increase in ORR kinetics due to the strongly anisotropic oxygen incorporation kinetics on  $\text{LSC}_{214}$  (100) surfaces exposed at the  $\text{LSC}_{214/113}$  interface. These results sug-

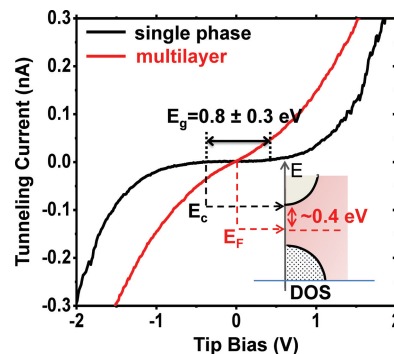


**Figure 6.** Comparison of tunneling spectra on  $\text{LSC}_{214}$  in single phase and in multilayer at 300 °C and oxygen pressure of  $10^{-3}$  mbar. While there is no gap present for the  $\text{LSC}_{214}$  surface in the multilayer structure, the band gap value,  $E_g$ , is about 0.8 eV for the single phase thin film structure. The energy difference between the Fermi level ( $E_F$ , corresponding to tip bias of 0 V) and the bottom of conduction band ( $E_C$ ) is around 0.4 eV on the single phase  $\text{LSC}_{214}$  surface. The reduction of  $E_C - E_F$  by 0.4 eV corresponds to a  $10^3$  times increase in the concentration of electrons in the conduction band of  $\text{LSC}_{214}$ , and thus, to a corresponding increase in the charge transfer kinetics on the surface.

gest that electronic activation of  $\text{LSC}_{214}$ , in concert with its anisotropically fast oxygen incorporation kinetics, is likely to be the key mechanism governing the fast oxygen reduction kinetics observed near  $\text{LSC}_{113/214}$  interfaces. Figure 7 schematically illustrates these mechanisms in the context of ORR reactivity of this model interface: (a) excess electron generation accompanying vacancy creation on/near the surface of  $\text{LSC}_{113}$  at high temperatures, (b) electron injection from  $\text{LSC}_{113}$  into  $\text{LSC}_{214}$ , (c) oxygen adsorption/dissociation on  $\text{LSC}_{214}$ , (d) electron charge transfer from  $\text{LSC}_{214}$  to the adsorbed oxygen and (e) fast oxygen incorporation in the [100] direction into the  $\text{LSC}_{214}$  (100) surface of the thin film.

We recognize that the  $\text{LSC}_{113/214}$  multilayer system in our paper has a different geometry compared to the  $\text{LSC}_{113/214}$  systems that were previously studied by SIMS<sup>[7,10]</sup> and EIS.<sup>[8,9]</sup> In fact, even among those different experiments reported, the

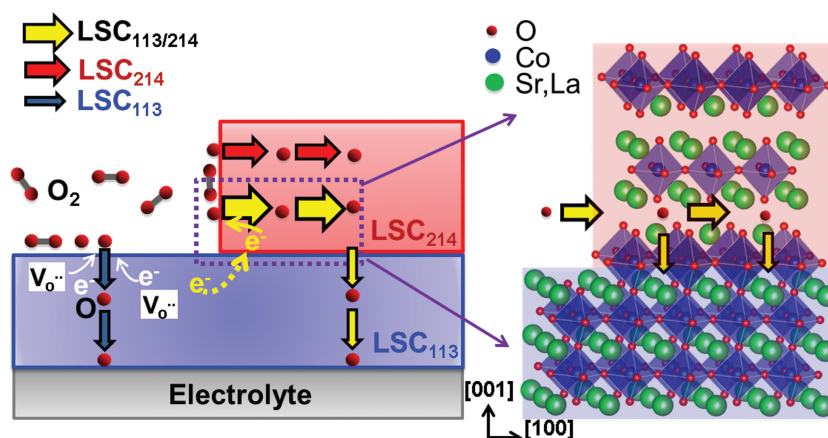


**Figure 7.** Mechanism that governs the enhancement of ORR activity at the interface of  $\text{LSC}_{113}$  and  $\text{LSC}_{214}$  layers. At high temperature, excess electrons from the reduced surface of  $\text{LSC}_{113}$  are injected across the interface into  $\text{LSC}_{214}$ , facilitating the charge transfer process at the  $\text{LSC}_{214}$  (100) surface. The electronic activation of  $\text{LSC}_{214}$ , concurrent with fast oxygen incorporation along [100] into  $\text{LSC}_{214}$ , leads to a stronger interaction of oxygen molecule on the  $\text{LSC}_{214}$  (100) surface, and thus, faster ORR kinetics at the  $\text{LSC}_{113/214}$  hetero-structure.



LSC<sub>113/214</sub> hetero-structures are different, ranging from dense thin films to porous structures. Despite the structural differences, the extremely high oxygen reduction activities are observed near the LSC<sub>113/214</sub> interface in all of those cases. Furthermore, nanoscale domains of LSC<sub>214</sub> in the VAN structures with LSC<sub>113/214</sub> hetero-interfaces without any FIB milling (in a parallel work of our group mentioned above)<sup>[32]</sup> exhibit the same electronic activation behavior at elevated temperatures. Based on these reasons, it is reasonable to suggest that the underlying reason for the very high ORR reactivity of the LSC<sub>113/214</sub> interface is intrinsic, and does not significantly depend on the interface geometry or the milling process to open the buried interfaces. Therefore, the electronic activation of LSC<sub>214</sub> induced by LSC<sub>113</sub> that we discovered in our model multilayer system should be applicable to those LSC<sub>113/214</sub> hetero-structures in the previously reported SIMS and EIS experiments.

This new knowledge, related to the electronic activation of one oxide phase by the defect states of a neighboring oxide phase, clarifies an important aspect of hetero-interfaces in determining the catalytic properties in oxide hetero-structures, especially at elevated temperatures. This new concept of “electronically coupled composite cathodes” serves to further accelerate the fast oxygen incorporation path on the RP phase A<sub>2</sub>BO<sub>4</sub> structured materials. For example, at 500 °C, RP oxygen surface exchange rates (via interstitial incorporation into the rock-salt layers) are reported to be fast, on the order of 10<sup>-7</sup> cm s<sup>-1</sup> along the (100) plane of single crystal<sup>[43]</sup> and thin film La<sub>2</sub>NiO<sub>4</sub>,<sup>[15]</sup> up to 10<sup>-6</sup> cm s<sup>-1</sup> for La<sub>2</sub>Ni<sub>1-x</sub>Co<sub>x</sub>O<sub>4</sub><sup>[44]</sup> and 10<sup>-7</sup> cm s<sup>-1</sup> for La<sub>2</sub>CuO<sub>4</sub>.<sup>[45]</sup> These values are comparable or better than those on the most widely studied and state-of-the-art perovskite oxides such as (Ba,Sr)(Co,Fe)O<sub>3</sub> (BSCF)<sup>[46]</sup> (10<sup>-6</sup> cm s<sup>-1</sup>) and LSC<sub>113</sub><sup>[47]</sup> (up to 10<sup>-7</sup> cm s<sup>-1</sup>). At the same time, because of the reduced structural symmetry, A<sub>2</sub>BO<sub>4</sub> materials have a larger energy gap and thus a lower density of available electrons compared to their perovskite counterparts.<sup>[18,19]</sup> When these A<sub>2</sub>BO<sub>4</sub> materials are interfaced with oxides that can be easily reduced, excess electrons are provided to the A<sub>2</sub>BO<sub>4</sub>, which in turn, are transferred to the oxygen molecule. This strengthens the interaction of oxygen with the surface, facilitates charge transfer to oxygen, and thus improves the ORR activity on A<sub>2</sub>BO<sub>4</sub>. The composite cathodes thus far considered for SOFCs are typically composed of a purely ionic conductor (e.g., yttria-stabilized zirconia (YSZ)) together with a largely electronic conductor (e.g., (La,Sr)MnO<sub>3</sub> (LSM)<sup>[48,49]</sup>). However, this comes at the expense of decreasing the effective surface area of the electrocatalyst. In the case of an electronically coupled composite cathode concept, the ORR activity enhancement is enabled by providing excess electrons to a phase that already exhibits relatively fast oxygen incorporation and diffusion.

### 3. Conclusion

We used a novel combination of in situ scanning tunneling microscopy/spectroscopy and focused ion beam milling on a model multilayer system to uncover the mechanism behind the very high reactivity of the LSC<sub>113/214</sub> hetero-interfaces to oxygen reduction at high temperature. The electronic structure information is directly and quantitatively tied to oxygen reduction

activity near the interface. We discovered that the wide-band-gap oxide, LSC<sub>214</sub>, is electronically activated through an interface coupling with LSC<sub>113</sub> at high temperatures (200–300 °C), while the LSC<sub>113</sub> in the ML structure behaves similar to its single-phase counterpart. Such electronic activation, concurrent with the anisotropic oxygen incorporation kinetics on the LSC<sub>214</sub>, is expected to facilitate charge transfer to oxygen near the LSC<sub>113/214</sub> interface, and is considered to be a key mechanism for the vastly accelerated ORR kinetics. Our results point towards electronically coupled oxide structures as novel cathodes. Our ability to probe the local electronic structure of oxide multilayer films at elevated temperatures also opens new opportunities for examining how electronic interactions at interfaces impact other important properties related to a wide range of technologies including electronic, magnet and superconducting devices.

### 4. Experimental Section

Pulsed laser deposition was performed using a KrF excimer laser with wavelength of 248 nm. The films were deposited at 700 °C under 10 mTorr oxygen pressure. After the growth process, the films were cooled down to room temperature in 2 Torr oxygen pressure to oxidize the films. The thickness of each LSC<sub>113</sub> and LSC<sub>214</sub> layer is 10 nm, with 10 modulations in the ML (200 nm thickness of ML in total). LSC<sub>214</sub> single phase films were grown under the same condition with thickness of 10 nm, as reference samples, to contrast the ML properties. LSC<sub>113</sub> reference data is taken from our previous work on LSC<sub>113</sub> single phase thin films.<sup>[12]</sup> FIB milling was carried out using the Helios Nanolab 600 dual beam FIB milling system. The Ga<sup>+</sup> beam current and acceleration were 100 pA and 30 kV, respectively. The angle between the beam and surface were carefully aligned to be less than 1°. This configuration resulted in exposed layer dimensions on the new surface close to 2.5 μm for each layer, which provides adequate spatial resolution for STM/STS measurements. After FIB sectioning, 1 keV Ar<sup>+</sup> ion sputtering was used to remove any potential Ga implantation into the material, followed by annealing in oxygen to remove any radiation damage.

A Physical Electronics Model 700 scanning nano-probe Auger Electron Spectrometer (AES) was used to spatially quantify the cation chemistry and the Ga content on the FIB-milled ML cross-section. The energy and current of incident electrons were 10 keV and 10 nA, respectively. Smoothing and differentiation of the AES spectra were performed using the Savitsky-Golay algorithm. Quantification of the AES differential spectra was carried out using peak-to-peak intensities of the tight scans of the La MNN, Sr LMM, and Co LMM Auger emissions. No residual Ga was found in the FIB-cut region after Ar sputtering, as shown in AES results in Supplementary Figure S2.

For identifying the crystal structure, the 2θ-ω scans were measured by a high resolution four circle Bruker D8 Discover diffractometer, equipped with a Göbel mirror, 4-bounce Ge (022) channel-cut monochromator, Eulerian cradle, and a scintillation counter, using Cu Kα<sub>1</sub> radiation.

A modified variable-temperature scanning tunneling microscope (VT-STM) (Omicron GmbH, Germany) was used to probe the surface morphology and to obtain surface electronic structure information with high spatial resolution at elevated temperatures (room temperature to 300 °C in this work) and in oxygen environment (10<sup>-3</sup> mbar in this work). STM was performed in constant-current mode using Pt/Ir tips prepared by chemical etching. A tip bias voltage of 2 V and feedback tunneling current of 50–500 pA were used during the measurements. The tunneling spectra were mapped spatially on the surface using the Matrix control system V 3.0, with a pixel size of 20 nm and 50 nm. A retractable oxygen doser placed near the STM stage in the chamber was used to directly expose the sample to oxygen during the STM/STS measurements. For surface cleaning and in situ measurements, samples

were heated using a pyrolytic boron nitride (PBN) heater. To obtain high quality images and tunneling spectra, the sample was cleaned prior to the STM/STS experiments by first sputtering the surface by low energy Ar<sup>+</sup> (0.5 keV) for 5 minutes, followed by heating in high purity oxygen at 450 °C and 10<sup>-3</sup> mbar pressure for 1 hour. This served to remove the water and carbon-related adsorbates from the surface due to air-exposure after film growth.

An Omicron EA 125 hemispherical analyzer and Omicron DAR 400 Mg/Al dual anode non-monochromated X-ray source were used for the x-ray photoelectron spectroscopy (XPS) measurements probing the surface chemistry. A key focus was measurement of the Co 2p emissions to determine the Co valence state. The XPS measurements were performed in the same ultra-high vacuum (UHV) chamber as that of the VT-STM. An Mg K X-ray source (1253.6 eV), operated at 300 W, was used for all the XPS data shown in this paper. Peak-fitting and chemical quantification were performed using the CasaXPS 2.3.15 software.

The crystal structure in Figure 7 is generated using the visualization software VESTA.

## Supporting Information

Supporting Information is available from the Wiley Online Library or from the author.

## Acknowledgements

Authors acknowledge the US-DOE - Basic Energy Sciences, Grant No. DE-SC0002633 for financial support. The FIB milling process and the X-ray diffraction and Auger electron spectroscopy measurements were performed at the Center of Materials Science and Engineering, an NSF MRSEC facility at MIT.

Received: January 8, 2013

Revised: February 18, 2013

Published online: May 8, 2013

- [1] H. A. Gasteiger, N. M. Markovic, *Science* **2009**, 324, 48.
- [2] S. B. Adler, *Chem. Rev.* **2004**, 104, 4791.
- [3] a) J. Suntivich, H. A. Gasteiger, N. Yabuuchi, H. Nakanishi, J. B. Goodenough, Y. Shao-Horn, *Nat. Chem.* **2011**, 3, 546; b) Y.-L. Lee, J. Kleis, J. Rossmeisl, Y. Shao-Horn, D. Morgan, *Energy Environ. Sci.* **2011**, 4, 3966.
- [4] W. Jung, H. L. Tuller, *Adv. Energy Mater.* **2011**, 1, 1184.
- [5] a) A. J. Jacobson, *Chem. Mater.* **2010**, 22, 660; b) A. Tarancon, M. Burriel, J. Santiso, S. J. Skinner, J. A. Kilner, *J. Mater. Chem.* **2010**, 20, 3799.
- [6] J. Garcia-Barriocanal, A. Rivera-Calzada, M. Varela, Z. Sefrioui, E. Iborra, C. Leon, S. J. Pennycook, J. Santamaria, *Science* **2008**, 321, 676.
- [7] M. Sase, F. Hermes, K. Yashiro, K. Sato, J. Mizusaki, T. Kawada, N. Sakai, H. Yokokawa, *J. Electrochem. Soc.* **2008**, 155, B793.
- [8] K. Yashiro, T. Nakamura, M. Sase, F. Hermes, K. Sato, T. Kawada, J. Mizusaki, *Electrochem. Solid State Lett.* **2009**, 12, B135.
- [9] E. J. Crumlin, E. Mutoro, S. J. Ahn, G. J. Ia O, D. N. Leonard, A. Borisevich, M. D. Biegalski, H. M. Christen, Y. Shao-Horn, *J. Phys. Chem. Lett.* **2010**, 1, 3149.
- [10] M. Sase, K. Yashiro, K. Sato, J. Mizusaki, T. Kawada, N. Sakai, K. Yamaji, T. Horita, H. Yokokawa, *Solid State Ion.* **2008**, 178, 1843.
- [11] a) J. Januschewsky, M. Ahrens, A. Opitz, F. Kubel, J. Fleig, *Adv. Funct. Mater.* **2009**, 19, 3151; b) S. B. Adler, *Solid State Ion.* **1998**, 111, 125.
- [12] Z. H. Cai, Y. Kuru, J. W. Han, Y. Chen, B. Yildiz, *J. Am. Chem. Soc.* **2011**, 133, 17696.
- [13] a) Y. A. Mastrikov, R. Merkle, E. Heifets, E. A. Kotomin, J. Maier, *J. Phys. Chem. C* **2010**, 114, 3017; b) R. Merkle, Y. A. Mastrikov, E. Heifets, E. A. Kotomin, M. Kukla, J. Maier, *ECS Trans.* **2009**, 25, 2753.
- [14] J. W. Han, B. Yildiz, *Energy Environ. Sci.* **2012**, 5, 8598.
- [15] M. Burriel, G. Garcia, J. Santiso, J. A. Kilner, J. C. C. Richard, S. J. Skinner, *J. Mater. Chem.* **2008**, 18, 416.
- [16] G. Kim, S. Wang, A. J. Jacobson, C. L. Chen, *Solid State Ion.* **2006**, 177, 1461; E. J. Opila, H. L. Tuller, B. J. Wuensch, J. Maier, *J. Am. Ceram. Soc.* **1993**, 76, 2363.
- [17] A. Kushima, D. Parfitt, A. Chroneos, B. Yildiz, J. A. Kilner, R. W. Grimes, *Phys. Chem. Chem. Phys.* **2011**, 13, 2242.
- [18] A. Petric, P. Huang, F. Tietz, *Solid State Ion.* **2000**, 135, 719.
- [19] V. V. Vashook, H. Ullmann, O. P. Olshevskaya, V. P. Kulik, V. E. Lukashevich, L. V. Kokhanovskij, *Solid State Ion.* **2000**, 138, 99.
- [20] B. Peng, G. Chen, T. Wang, J. Zhou, J. J. Guo, Y. H. Cheng, K. Wu, *J. Power Sources* **2012**, 201, 174.
- [21] A. Yamada, Y. Suzuki, K. Saka, M. Uehara, D. Mori, R. Kanno, T. Kiguchi, F. Mauvy, J. C. Grenier, *Adv. Mater.* **2008**, 20, 4124.
- [22] L. P. Sun, Q. Li, L. H. Huo, H. Zhao, G. Y. Zhang, N. Lin, J. P. Viricelle, C. Pijolat, *J. Power Sources* **2011**, 196, 5835.
- [23] A. Ohtomo, D. A. Muller, J. L. Grazul, H. Y. Hwang, *Nature* **2002**, 419, 378.
- [24] J. Chakhalian, J. W. Freeland, H. U. Habermeier, G. Cristiani, G. Khaliullin, M. van Veenendaal, B. Keimer, *Science* **2007**, 318, 1114.
- [25] a) A. Kumar, F. Ciucci, A. N. Morozovska, S. V. Kalinin, S. Jesse, *Nat. Chem.* **2011**, 3, 707; b) M. W. Louie, A. Hightower, S. M. Haile, *ACS Nano* **2010**, 4, 2811.
- [26] M. Basletic, J. L. Maurice, C. Carretero, G. Herranz, O. Copie, M. Bibes, E. Jacquet, K. Bouzehouane, S. Fusil, A. Barthelemy, *Nat. Mater.* **2008**, 7, 621.
- [27] T. Y. Chien, J. A. Liu, J. Chakhalian, N. P. Guisinger, J. W. Freeland, *Phys. Rev. B* **2010**, 82, 041101.
- [28] I. Valov, I. Sapezanskaia, A. Nayak, T. Tsuruoka, T. Bredow, T. Hasegawa, G. Staikov, M. Aono, R. Waser, *Nat. Mater.* **2012**, 11, 530–535.
- [29] A. Nayak, T. Tamura, T. Tsuruoka, K. Terabe, S. Hosaka, T. Hasegawa, M. Aono, *J. Phys. Chem. Lett.* **2010**, 1, 604–608.
- [30] Y. Kuru, H. Jalili, Z. H. Cai, B. Yildiz, H. L. Tuller, *Adv. Mater.* **2011**, 23, 4543.
- [31] A. Kushima, S. Yip, B. Yildiz, *Phys. Rev. B* **2010**, 82, 115435.
- [32] W. MA, J. J. Kim, Y. Kuru, Z. Cai, Y. Chen, H. L. Tuller, B. Yildiz, **2012** Unpublished.
- [33] E. Dagotto, *Science* **2005**, 309, 257.
- [34] M. J. Gadre, Y. L. Lee, D. Morgan, *Phys. Chem. Chem. Phys.* **2012**, 14, 2606.
- [35] C. W. Schneider, M. Esposito, I. Marozau, K. Conder, M. Doebeli, Y. Hu, M. Mallepell, A. Wokaun, T. Lippert, *Appl. Phys. Lett.* **2010**, 97, 192107.
- [36] R. A. De Souza, *Phys. Chem. Chem. Phys.* **2009**, 11, 9939.
- [37] a) M. V. Ganduglia-Pirovano, A. Hofmann, J. Sauer, *Surf. Sci. Rep.* **2007**, 62, 219; b) T. Nishimura, A. Ikeda, H. Namba, T. Morishita, Y. Kido, *Surf. Sci.* **1999**, 421, 273.
- [38] K. Katsiev, B. Yildiz, K. Balasubramaniam, P. A. Salvador, *Appl. Phys. Lett.* **2009**, 95, 092106.
- [39] Y. Chen, W. C. Jung, Z. Cai, J. J. Kim, H. Tuller, B. Yildiz, *Energy Environ. Sci.* **2012**, 5, 7979.
- [40] a) N. A. Deskins, R. Rousseau, M. Dupuis, *J. Phys. Chem. C* **2010**, 114, 5891; b) M. T. Greiner, M. G. Helander, W. M. Tang, Z. B. Wang, J. Qiu, Z. H. Lu, *Nat. Mater.* **2012**, 11, 76.

- [41] R. F. Pierret, *Semiconductor Device Fundamentals*, Pearson Education, 1996.
- [42] a) P. W. Fry, I. E. Itskevich, D. J. Mowbray, M. S. Skolnick, J. J. Finley, J. A. Barker, E. P. O'Reilly, L. R. Wilson, I. A. Larkin, P. A. Maksym, M. Hopkinson, M. Al-Khafaji, J. P. R. David, A. G. Cullis, G. Hill, J. C. Clark, *Phys. Rev. Lett.* **2000**, *84*, 733; b) M. E. Messing, J. Wong-Leung, Z. Zanolli, H. J. Joyce, H. H. Tan, Q. Gao, L. R. Wallenberg, J. Johansson, C. Jagadish, *Nano Lett.* **2011**, *11*, 3899.
- [43] J. M. Bassat, P. Odier, A. Villesuzanne, C. Marin, M. Pouchard, *Solid State Ion.* **2004**, *167*, 341.
- [44] C. N. Munnings, S. J. Skinner, G. Amow, P. S. Whitfield, I. J. Davidson, *Solid State Ion.* **2005**, *176*, 1895.
- [45] E. Boehm, J. M. Bassat, P. Dordor, F. Mauvy, J. C. Grenier, P. Stevens, *Solid State Ion.* **2005**, *176*, 2717.
- [46] L. Wang, R. Merkle, J. Maier, T. Acarturk, U. Starke, *Appl. Phys. Lett.* **2009**, *94*.
- [47] R. A. De Souza, J. A. Kilner, *Solid State Ion.* **1999**, *126*, 153.
- [48] E. P. Murray, S. A. Barnett, *Solid State Ion.* **2001**, *143*, 265.
- [49] A. V. Virkar, J. Chen, C. W. Tanner, J. W. Kim, *Solid State Ion.* **2000**, *131*, 189.